Effects of a capillary transition zone on the stability of a diffusive boundary layer

Maria T. Elenius*

Uni CIPR, PO Box 7800, 5020 Bergen, Norway and Department of Mathematics, University of Bergen, PO Box 7803, 5020 Bergen, Norway
*Corresponding author: maria.elenius@uni.no

Jan M. Nordbotten and Henrik Kalisch

Department of Mathematics, University of Bergen, PO Box 7803, 5020 Bergen, Norway
jan.nordbotten@math.uib.no   henrik.kalisch@math.uib.no

In geological storage of carbon dioxide (CO_2), the buoyant CO_2 plume eventually accumulates under the caprock. Due to interfacial tension between the CO_2 phase and the water phase, a capillary transition zone develops in the plume. This zone contains supercritical CO_2 as well as water with dissolved CO_2. Under the plume, a diffusive boundary layer forms. We study how cross-flow between the capillary transition zone and the diffusive boundary layer affects gravitational stability of the diffusive boundary layer. Linear stability analysis shows that this cross-flow has no significant effect on the selection of the critical mode. However, interaction with the capillary transition zone enhances the instability of the boundary layer, such that the onset of instabilities occurs earlier, when the diffusive boundary layer is thinner. The onset time may be reduced by a factor of five, which corresponds to the thickness of the diffusive boundary layer at onset being reduced by a factor of two. This reduced thickness of the boundary layer at onset can be interpreted in terms of a reduced portion of the critical mode that must 'fit' inside the boundary layer when the other portion of the mode is confined within the capillary transition zone. Direct numerical simulations for the non-linear regime show that the mass transfer rate can be enhanced up to four times when the cross-flow is accounted for. This increase is related to advective inflow of CO_2-saturated water across the interface. Therefore, the contribution from dissolution to the safety of geological storage of CO_2 begins earlier and can be considerably larger than showed by estimates that neglect the capillary transition zone.

Keywords: stability analysis, CO_2 storage, capillary transition zone.

1. Introduction

In recent years, geological storage of carbon dioxide (CO_2) has attained focus as a mitigation strategy for the excess accumulation of this greenhouse gas in the Earth's atmosphere (IPCC, 2005). When the supercritical CO_2 is injected into an aquifer, it rises and spreads along the caprock and eventually dissolves into the resident water that it comes into contact with. A diffusive boundary layer of water with dissolved CO_2 develops under the plume and above the lighter unaffected water, see Fig. 1. After a period of stability, the boundary layer becomes unstable and density-driven convection begins. This instability has been noted to greatly enhance the dissolution rate of CO_2 and is therefore an important factor of safe storage of CO_2 in deep saline aquifers.

An accurate solution for the dissolution of CO_2 in homogeneous aquifers was provided by Riaz *et al.* (2006). However, as they note, there may be an influence of capillary forces which is not included in their work. Indeed, large-scale simulations of a CO_2 plume show that CO_2-saturated water in the
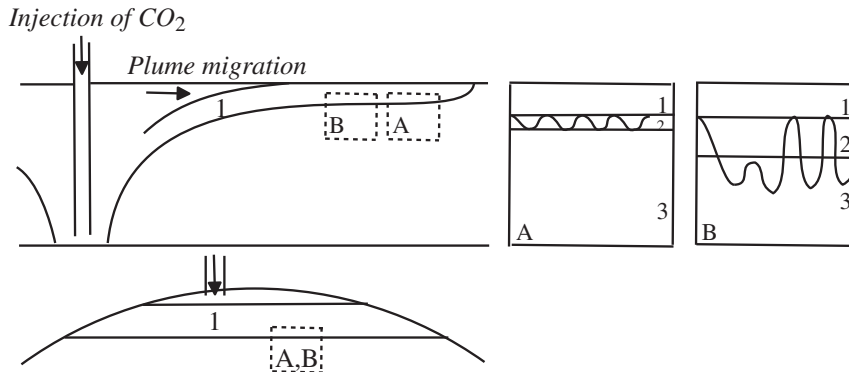
Fig. 1. Schematic view of the flow regimes: (1) capillary transition zone with mobile CO_2-saturated water phase and mobile CO_2 phase; (2) diffusive boundary layer with CO_2 concentration between some very small value ϵ and the solubility limit; and (3) water with CO_2 concentration smaller than ϵ from diffusion. Higher concentrations may occur in perturbations that have grown into fingers. The time-evolution is: (A) early in the development of the diffusive boundary layer. Perturbations are small and independent of each other (linear regime); and (B) later in the development of the diffusive boundary layer. The perturbations have grown and are interacting with each other (non-linear regime). The analysis performed here applies when the interface between the capillary transition zone and the water is (nearly) horizontal and the depth of the interface is (nearly) stationary. This can e.g. occur in the post-injection period of injection operations into structural traps, or in the injection- and post-injection periods of injection without structural traps, away from the injection well.

capillary transition zone does participate in the convection (Elenius, 2011). The influence of the capillary transition zone on the stability is at least two-fold: it changes the flow direction at the interface between the two-phase and single-phase regions, which may lead to differences in the linear regime, and it acts as a source of CO_2-saturated water, which may have an influence in the non-linear regime.

Let us first look at a simplified system where the interface between the capillary transition zone and the diffusive boundary layer is horizontal. Assume further that the permeability field is homogeneous but with a reduced effective permeability for the water above the interface due to the interactions between the phases. For the sake of analytical tractability, we make the further simplifying assumption that there is a sharp transition in the permeability. We call the permeabilities below and above the interface K_1 and K_2, respectively. The angles between the normal to the interface and the flow direction are denoted α_1 below the interface and α_2 above the interface. Then these angles and permeabilities are related by the tangent law (see e.g. Pinder & Celia, 2006),

$$\tan \alpha_1 = \frac{K_1}{K_2} \tan \alpha_2. \tag{1}$$

In the investigations by Riaz *et al.* (2006) and many others, it was assumed that there is no flow across the interface. Therefore, the flow at the interface was assumed to be horizontal ($\alpha_1 = \pi/2$). This is achieved when $K_2 \to 0$, i.e. when there is infinite resistance for water to flow into the capillary transition zone. The other endpoint occurs when there is no resistance to flow inside the capillary transition zone, $K_2 \to \infty$, in which case $\alpha_1 \to 0$, representing purely vertical flux at the interface. We present solutions for the linear regime (linear stability analysis) and for the non-linear regime (direct numerical simulations), which account for this other endpoint of the influence of the capillary transition zone and/or changes in the medium properties. The single-phase water region is studied and the interface is treated as a top boundary where the flow direction is vertical. We also derive the general boundary condition for any K_2 and show how solutions to this case may be obtained.

A recent paper by Slim & Ramakrishnan (2010) also considers the effects of the capillary transition zone. Their analysis differs from the one presented here in that they consider arbitrary perturbations of the initial conditions, while our analysis focuses on perturbations at the interface. Furthermore, they include no numerical study of the non-linear regime, and do not investigate the upscaled parameters needed for field-scale simulations. While arbitrary perturbations of the base state lead to faster establishment of unstable modes, perturbations localized at the interface may yield a more realistic rendering of the physical situation.

The influence of the top boundary condition on onset of convection was previously studied by Foster (1968). However, there was no vertical component of the flux at the top boundary. Nield & Bejan (2006) studied the effect of the vertical versus horizontal flux at the boundary for the thermal convection problem with a static linear base temperature gradient. They found that the critical Rayleigh number, which is an indicator of the stability of the system, was reduced by a factor 2.3 with the vertical flux (constant pressure boundary). Other analytical solutions for density-driven convection of dissolved compounds assume single-phase flow with horizontal velocities at the top boundary. Lindeberg & Wessel-Berg (1997) calculated stability numbers for typical high permeability aquifers of the North Sea and concluded that density-driven convection could occur in this type of CO_2 storage. Ennis-King *et al.* (2005) and Xu *et al.* (2006) performed linear stability analysis for the anisotropic porous medium for single-phase water. Riaz *et al.* (2006) presented a linear stability analysis for homogeneous aquifers based on the dominant mode of the diffusion operator, and also used the quasi-steady-state approximation and performed numerical simulations. Hidalgo & Carrera (2009) performed numerical simulations to study the effect of dispersion and concluded that dispersion reduces the onset time compared with pure diffusion, although mass transfer was not much affected. Heterogeneity effects were studied numerically by Farjazadeh *et al.* (2011). Pau *et al.* (2010) noted that for homogeneous media, dimensionality (2D versus 3D) has a rather small effect on convective enhanced mass transfer, as shown with high-resolution numerical simulations. Special focus on the mass transfer rate was also attained by Hesse (2008) and Pruess & Zhang (2008). Recently, Neufeld *et al.* (2010) presented a new relation between the mass transfer rate and the Rayleigh number, verified by experiments and numerical simulations. A combination of experimental and numerical work was also performed by Kneafsey & Pruess (2010), related to Hele-Shaw cells.

2. Linear stability analysis

2.1 *Model problem for the linear regime*

Here, we shall first give the equations for the water phase in two sub-domains; the upper region representing the capillary transition zone and the lower region representing the region with single-phase water. Later, we shall use the interface as a boundary condition and only treat the lower region. For the lower region, we assume Boussinesq flow with a linear density dependence on concentration and gravity pointing in the positive *z*-direction:

$$\mathbf{u} = -\frac{K_1}{\mu}(\nabla p - \rho \mathbf{g}), \tag{2}$$

$$\phi\, \partial_t c = -\mathbf{u} \cdot \nabla c + \phi D \nabla^2 c, \tag{3}$$

$$\nabla \cdot \mathbf{u} = 0, \tag{4}$$

$$\rho = \rho_0 + \Delta\rho\, c. \tag{5}$$

Here $\mathbf{u}$ is the Darcy flux, p is the pressure, c is the normalized concentration of CO_2, ρ_0 is the density of pure water and ρ is the density of water with concentration c. The material properties are assumed constant. In particular, K_1 is the permeability, μ is the viscosity, ϕ is the porosity and D is the diffusion coefficient. Experimental data (Yang & Gu, 2006) confirm a linear relation between concentration and density for CO_2 storage.

For the upper region, the concentration is unity and the equations for the water phase reduce to

$$\mathbf{u} = -\frac{K_2}{\mu}(\nabla p - (\rho_0 + \Delta\rho)\mathbf{g}), \tag{6}$$

$$\nabla \cdot \mathbf{u} = 0, \tag{7}$$

where K_2 is the effective permeability of the water phase in this two-phase region.

We study the problem in two spatial dimensions where x is the horizontal direction and z is the downward pointing vertical direction. The interface is located at $z = 0$ for all times. The stationary interface is motivated by the fast establishment of equilibrium between the phases (Ennis-King & Paterson, 2003). Furthermore, by mass balance arguments, it is easy to see that dissolution causes only relatively slow receding motion of the transition zone. The initial conditions are given by $c(x, z > 0, 0) = 0$, $c(x, z < 0, 0) = 1$ and $\mathbf{u}(x, z, 0) = 0$, where $\mathbf{u} = (u, w)$, apart for small perturbations explained below.

The conditions at the interface and lower boundary are,

$$c(x, 0, t) = 1, \quad [[p(x, 0, t)]] = 0, \quad [[w(x, 0, t)]] = 0, \tag{8}$$

$$c(x, H, t) = 0, \quad w(x, H, t) = 0, \tag{9}$$

where H is the thickness of the lower layer as shown in Fig. 2 and $[[\ ]]$ represents a jump of the variable. The equations are scaled with the characteristic velocity $u_c = K\Delta\rho g/\mu$, length $l_c = D\phi/u_c$ and time $t_c = D\phi^2/u_c^2$. In addition, the pressure is scaled such that the dimensional pressure p is obtained from the non-dimensional pressure P by the relation $p = D\mu\phi/K(P + \rho_0/\Delta\rho\, z)$. The non-dimensional form of the equations is for the lower layer,

$$\mathbf{u} = -(\nabla P - c\mathbf{e}_z), \tag{10}$$

$$\partial_t c = -\mathbf{u} \cdot \nabla c + \nabla^2 c, \tag{11}$$
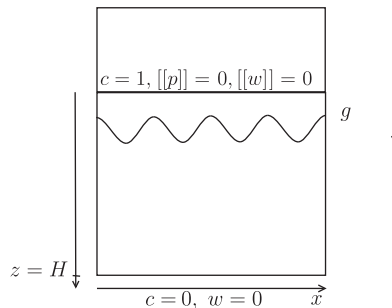
$$\nabla \cdot \mathbf{u} = 0, \tag{12}$$

FIG. 2. Interface and boundary conditions.

and for the upper layer

$$\mathbf{u} = -\mathscr{K}(\nabla P - \mathbf{e}_z), \tag{13}$$

$$\nabla \cdot \mathbf{u} = 0, \tag{14}$$

where $\mathscr{K} = K_2/K_1$. We then write the concentration, pressure and velocities as a sum of base states and perturbation components as shown here for the concentration,

$$c(x, z, t, k) = c_0(z, t) + \hat{c}(z, t, k)\, e^{ikx}, \tag{15}$$

where k is the horizontal wavenumber and $\hat{c}(z, t, 0) = \hat{w}(z, t, 0) = 0$. The base state is described by

$$c_0(z, t) = 1 - \mathrm{erf}(z/(2\sqrt{t})), \quad (z > 0) \tag{16}$$

$$c_0(z, t) = 1, \quad (z \leqslant 0) \tag{17}$$

$$u_0(z, t) = w_0(z, t) = 0, \tag{18}$$

where the first condition follows from mass balance, the second condition is motivated by mass transfer of CO_2 from the CO_2 phase to the water phase in the upper layer and the third condition has been chosen for convenience.

Next, we wish to replace the no-jump conditions in (8) with an explicit top boundary condition to be used for the lower region. With zero base velocities, we obtain $\hat{w} = -\partial_z \hat{P} + \hat{c}$ for the lower layer $\hat{w} = -\mathscr{K} \partial_z \hat{P}$ and for the upper layer. In the upper layer, solving the Laplace equation for the pressure with periodic functions in the lateral direction and vanishing velocities as $z \to -\infty$ gives $\hat{P}(z, t, k) = \hat{P}(0, t, k)\, e^{kz}$, i.e. $\partial_z \hat{P} = k\hat{P}$ and $\hat{w} = -\mathscr{K}k\hat{P}$. Then the interface conditions show that

$$\mathscr{K}k\hat{P} = \partial_z \hat{P}. \tag{19}$$

By use of (12) this can be rewritten it in the terms of the vertical velocity perturbation as

$$\partial_z \hat{w} = \frac{k}{\mathscr{K}} \hat{w}. \tag{20}$$

Using the ansatz (15) and the specific form of the base state, a system of two linear partial differential equations in c and w appears. Since the base concentration c_0 is self-similar in the variable $\xi = z/(2\sqrt{t})$, a coordinate transformation from (z, t) to (ξ, t) is appropriate.

Finally, in the new variables (ξ, t), the system of perturbation equations to be solved is

$$\left(\frac{1}{4t} \frac{\mathrm{d}^2}{\mathrm{d}\xi^2} - k^2 \right) \hat{w} = -k^2 \hat{c}, \tag{21}$$

$$\frac{\partial \hat{c}}{\partial t} - \frac{1}{t}(\mathscr{L} - k^2 t)\hat{c} = \sqrt{\frac{1}{\pi t}}\, e^{-\xi^2} \hat{w}, \tag{22}$$

where the operator $\mathscr{L}$ is given by $\mathscr{L} = \frac{1}{4}(\partial^2/\partial \xi^2) + (\xi/2)(\partial/\partial \xi)$. These equations are supplemented with the boundary conditions

$$\hat{c}(\xi = 0, t, k) = 0, \quad \partial_\xi \hat{w}(\xi = 0, t, k) = \frac{2k\sqrt{t}}{\mathscr{K}} \hat{w}(\xi = 0, t, k), \tag{23}$$

$$\hat{c}(\xi \to \infty, t, k) = 0, \quad \hat{w}(\xi \to \infty, t, k) = 0. \tag{24}$$

The special case $\mathscr{K} \to \infty$ corresponds to vertical velocities at the interface because $\partial_z w = 0$ implies that $\partial_x u = 0$, and without base velocities this means that $u = 0$.

The focus of the investigation will be on the exponential growth rate of the perturbations, defined by

$$\sigma(\xi, t, k) = \frac{\partial \hat{c}/\partial t}{\hat{c}}. \tag{25}$$

To obtain a complete picture of the growth of the instability, both pointwise and integral values of σ will be found. In Section 2.3, we describe an analytical method for obtaining σ. In Section 2.4, results from the analytical method are discussed and compared with numerical solutions to the IVP. For the latter, the problem is discretized with a fully implicit scheme that is first order in t and second order in ξ. The step sizes in t and ξ and the streamwise domain size are chosen such that the estimated combined error in σ is less than 1×10^{-4}.

2.2 *Initial condition*

Next, the initial condition will be discussed and its effects on the growth of the perturbation will be established. As pointed out by Pau *et al.* (2010), in the context of the Boussinesq approximation, the initial perturbation cannot be introduced in the permeability field. Instead, we initiate the perturbations by means of the concentrations. Since the perturbation $\hat{c}$ satisfies a homogeneous Dirichlet boundary condition, the Hermite polynomials of odd order can be used to expand $\hat{c}$. We use the Hermite polynomials (Folland, 1992) defined by

$$H_n(\xi) = (-1)^n e^{\xi^2} \frac{d^n}{d\xi^n}(e^{-\xi^2}). \tag{26}$$

This is a natural choice since the functions $\phi_n(\xi) = e^{-\xi^2} H_n(\xi)$ are eigenfunctions of the operator $\mathscr{L}$ on the domain $[0, \infty)$. Thus, using the weight function $\omega = e^{-\xi^2}$, the function $\hat{c}$ can be expanded by

$$\hat{c}(\xi, t) = \sum_{n=1,3,5,\dots} A_n(t) \phi_n(\xi), \tag{27}$$

where the coefficients are given by

$$A_n(t) = \frac{\int_0^\infty \hat{c}(\xi, t) \mathscr{H}_n(\xi) \omega(\xi) \, d\xi}{\int_0^\infty \mathscr{H}_n(\xi) \mathscr{H}_n(\xi) \omega(\xi) \, d\xi}. \tag{28}$$

In the work of Riaz *et al.* (2006), visual inspection of the solutions of the IVP for an arbitrary initial condition indicated that if the velocity field is assumed purely horizontal at the top boundary, then arbitrary streamwise initial perturbations converge to the mode $\hat{c}(\xi, t) = A_1(t)\xi e^{-\xi^2}$ rather quickly,
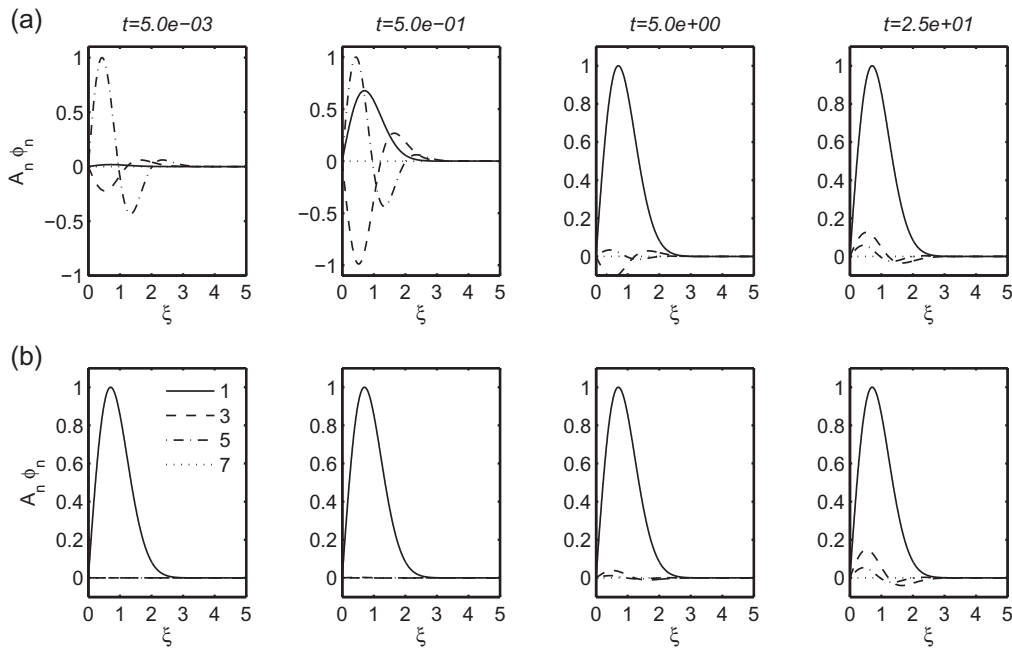
FIG. 3. Normalized $A_n\phi_n$ from the decomposed IVP solution of $\hat{c}$ for subsequent non-dimensional times with (a) an arbitrary initial condition and (b) the first mode as initial condition (k=0.08). The effect of the initial condition is negligible after non-dimensional time $t \approx 25$. Modes $n > 7$ are negligible and therefore not shown.

and in particular on a shorter time scale than the onset of convection. Note that this corresponds to the Hermite polynomial of degree 1.

Using a purely vertical velocity field at the top boundary condition changes the convergence of the initial perturbation of $\hat{c}$ towards the first mode. The convergence in this situation is now analysed by comparing the coefficients in the Hermite expansion (27) in the case where an arbitrary perturbation in the streamwise direction is specified to the case where initial data of the form $\hat{c} = A_1\phi_1$ are given. As can be clearly seen in Fig. 3, the effect of the initial condition on the streamwise perturbations disappears at $t \approx 25$ ($k = 0.08$). At this time, the first mode is dominant. On the other hand, it should be noted that there is a contribution from higher modes even when the system is initialized with the first mode only. This fact can be explained by the dependence on ξ of the right-hand side of (22). However, as Fig. 3 suggests, this effect can be neglected in a first approximation. In light of the above, only the first mode is used as the initial condition for the numerical solution of the linearized IVP.

Note that at $t \approx 0$ any finite ξ corresponds to $z \approx 0$. Therefore, our initial perturbations are restricted to the infinitesimal diffusion layer. This is physically relevant since we expect the system to be most dynamic at the interface to the two-phase region. In comparison, Slim & Ramakrishnan (2010) used the most unstable initial perturbation which is not constrained within the diffusion layer. In this way, they found a more unstable initial mode giving rise to earlier onset.

2.3 *Dominant mode method*

Since it appears that the first mode in the Hermite expansion is always dominant, one may also consider an analysis which focuses exclusively on this dominant mode. Such an approach has been used by

Robinson (1976) and Riaz *et al.* (2006), and we aim to supplement the numerical analysis of the IVP by presenting an analytical solution to the IVP with $\hat{c}$ restricted to the first mode. As was explained in Riaz *et al.* (2006), if only the dominant mode with eigenvalue -1 is used in (22), then an integration across the domain yields the following expression for the growth rate of the dominant mode.

$$\sigma = \frac{\mathrm{d}A_1/\mathrm{d}t}{A_1} = -\frac{1}{t} - k^2 + \frac{1}{\sqrt{\pi t}} \frac{\int_0^\infty \mathrm{e}^{-\xi^2} \hat{w}/A_1 \, \mathrm{d}\xi}{\int_0^\infty \xi \, \mathrm{e}^{-\xi^2} \, \mathrm{d}\xi}. \tag{29}$$

From (21), we solve for $\hat{w}$ and obtain,

$$\hat{w} = A_1 k^2 t \sqrt{\pi} \left\{ \mathrm{e}^{2k\xi\sqrt{t}} \left(\frac{1}{2} \mathrm{e}^{k^2 t} \mathrm{erf}(\xi + k\sqrt{t}) + \frac{B_1}{k\sqrt{\pi t}} \right) \right.$$
$$\left. - \mathrm{e}^{-2k\xi\sqrt{t}} \left(-\frac{1}{2} \mathrm{e}^{k^2 t} \mathrm{erf}(\xi - k\sqrt{t}) + \frac{B_2}{k\sqrt{\pi t}} \right) \right\}, \tag{30}$$

where the boundary conditions (23) and (24) are fulfilled by choosing

$$B_1 = -\frac{k\sqrt{\pi t}}{2} \mathrm{e}^{k^2 t}, \tag{31}$$

$$B_2 = \frac{1 - \mathscr{K}}{1 + \mathscr{K}} B_1 - \frac{\mathscr{K}}{\mathscr{K} + 1} (k\sqrt{\pi t} \, \mathrm{e}^{k^2 t} \mathrm{erf}(k\sqrt{t}) + 1). \tag{32}$$

2.4 *Results for the linear regime*

The analysis presented in Section 2.3 is valid for arbitrary $\mathscr{K}$. In order to highlight the effect of the two-phase region, which was not considered by Riaz *et al.* (2006), we will now focus on the opposite endpoint of the problem, namely the case where $\mathscr{K} \to \infty$.

The growth rates obtained from the numerical solution of the IVP and from the dominant mode solution are presented in Fig. 4(a). For comparison, solutions with horizontal top boundary velocity are presented in Fig. 4(b). Note first that the growth rates are not uniquely defined, because they vary in the streamwise direction. Growth rates computed with three different definitions are shown in Fig. 4. The squares indicate growth rates computed using the maximum value taken over ξ. The triangles indicate growth rates computed at the maximum of $\hat{c}$. The circles indicate growth rates computed using the integral definition $\sigma = \int \partial \hat{c}/\partial t \, \mathrm{d}\xi / \int \hat{c} \, \mathrm{d}\xi$. In the following, the dominant mode results are referred to if nothing else is specified. With the vertical top boundary flux, the onset of instability occurs much sooner than with horizontal flux at the top boundary. Indeed, Fig. 4 shows that the transition time is smaller by a factor of five in the first case. Since the analysis surrounding Fig. 3 showed that the effect of the initial condition is very weak after $t \approx 25$, which is before the onset of instability, we conclude that the exact form of our initial data does not have a significant effect on the time of the onset of instability *as long as it is constrained within the diffusion layer*, cf. Section 2.2. It can also be seen from Fig. 4 that the wavenumber of the most unstable mode does not show a strong dependence on the type of top boundary condition used for the velocity.

In Fig. 5(a), the growth rate corresponding to the gravest horizontal mode is shown as a function of time. Figure 5(b) displays the wavenumber $k_{\max}$ of the gravest horizontal mode as a function of time, as well as the short- and longwave cutoff modes k_S and k_L which confine the region of the positive growth. The non-dimensional onset time is $t_c = 31$ and the critical wavenumber is $k_c = 0.086$. For comparison,
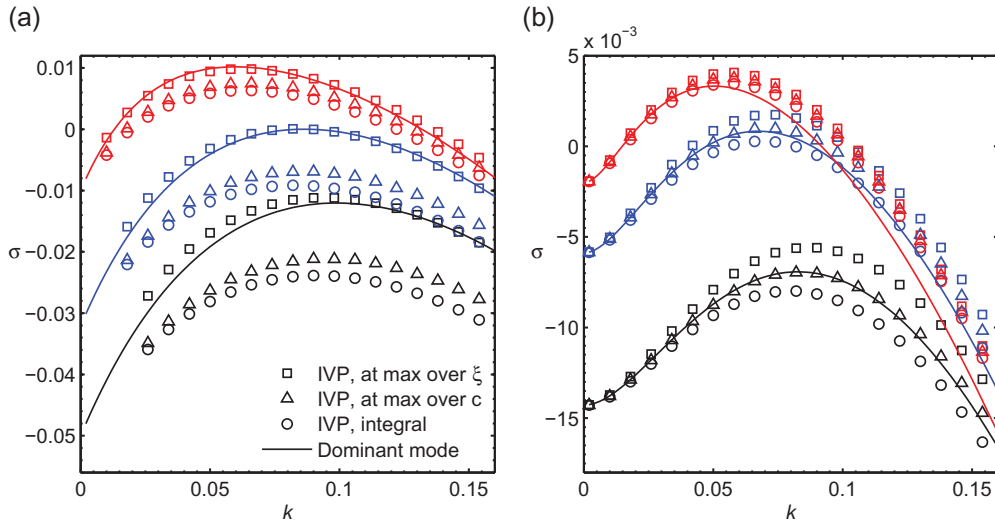
FIG. 4. (a) Exponential growth rate for our investigation with a vertical flux at the top boundary. The colours correspond to non-dimensional times $t = 20$ (black), $t = 31$ (blue) and $t = 100$ (red). (b) Growth rates reproduced from Riaz *et al.* (2006) with horizontal flux at the top boundary. The colours correspond to non-dimensional times $t = 70$ (black), $t = 170$ (blue) and $t = 500$ (red).
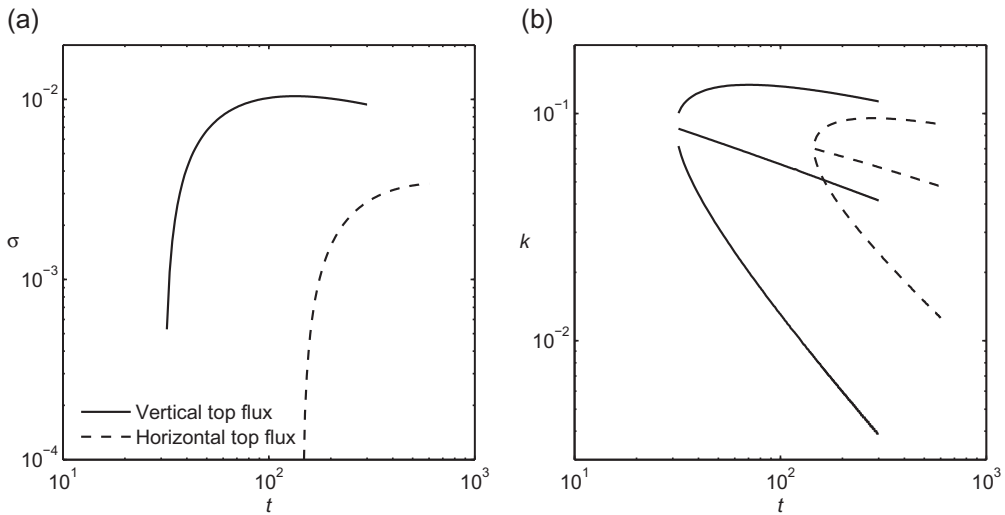
FIG. 5. (a) Maximum growth rate computed with the dominant mode method for the two sets of top boundary conditions. (b) Wavenumbers computed with the dominant mode method, corresponding to the maximum growth rate k_{max}, with the short-wave cutoff k_S above and the longwave cutoff k_L below.

results from the investigation of Riaz *et al.* (2006) are reproduced in the same figures. Their onset time is about five times larger ($t_c = 146$) and their critical wavenumber is slightly lower ($k_c = 0.07$). In addition, the maximum growth rate is three times larger with our vertical top boundary flux. However,

the growth rate also decays faster after the time when the maximum is reached. The data displayed in Fig. 5 show that it then decays as $\approx t^{1/3}$ instead of as $\approx t^{1/4}$ with the horizontal flux boundary condition. In addition, $k_{\max}$ decays as $\approx t^{1/3}$ rather than $\approx t^{1/4}$. This means that the wavelength corresponding to the most unstable mode increases slightly faster with the vertical top boundary flux.

3. Non-linear stability investigation

In this section, the focus is on the effect of the capillary transition zone on flow behaviour in the non-linear regime, where the linear stability analysis does not necessarily apply. For this regime, the problem is solved using numerical simulations for a 2D square domain with the finite-volume simulator d^3f (Fein, 1998; Johannsen, 2004).

3.1 *Model problem for the non-linear regime*

For the non-linear regime, we solve the full set of (10)–(12). Dirichlet boundary conditions are applied at the top boundary,

$$P(x, 0, t) = P_1, \tag{33}$$

$$c(x, 0, t) = 1. \tag{34}$$

The constant pressure P_1 in (33) corresponds to the vertical flux at the top boundary since $\partial_x P = 0$. At all other boundaries, no-flow boundary conditions are applied,

$$\mathbf{n} \cdot \mathbf{u} = 0, \tag{35}$$

$$\mathbf{n} \cdot (\mathbf{u}c - \nabla c) = 0, \tag{36}$$

where $\mathbf{n}$ is the normal vector to the respective boundary. Initially, the pressure is static and the concentration is zero within the domain except for small random perturbations described in the next section.

For comparison, we also perform simulations applying boundary condition (35) instead of (33) also at the top boundary. This corresponds to the horizontal flux at the top boundary. With those boundary conditions, the pressure is only determined up to a constant. Therefore, we prescribe the pressure at the bottom right corner.

3.2 *Numerical scheme*

The governing equations are discretized in time with the second-order Alexander scheme. For space discretization, we first tried the second-order central difference scheme. However, problems arose due to the non-monotonicity of this scheme when used with boundary condition (33). Therefore, we apply a first-order partial-upwinding scheme instead. The non-linear system is solved with Newton's method and the linear sub-problems are solved with the biconjugate gradient stabilized method (BiCGSTAB), with a multigrid preconditioner and overlapping block Gauss–Seidel smoother. In the non-dimensional setting, the time step size is 48, the cell sizes are 3.9×3.9 and the domain size is 2000×2000. A convergence study showed that we obtain a good approximation to the continuous solution of the equations with these choices, with small effects of the lateral and bottom boundaries. We initiate the simulations with small random perturbations $c \in 1 \times 10^{-6}[-1 \quad 1]$ on the first grid points below the top boundary, with consistent perturbations in the pressure and flux field by (10)–(12).
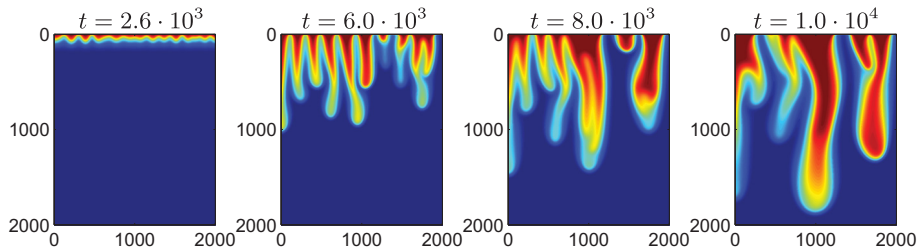
FIG. 6. Concentration of CO_2 in the domain with vertical top boundary flux.
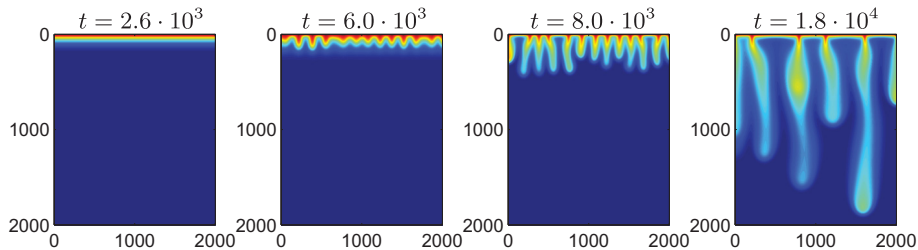
FIG. 7. Concentration of CO_2 in the domain with horizontal top boundary flux. Note that the last time shown differs from the previous figure.

3.3   *Results for the non-linear regime*

In Figs 6 and 7, we show concentrations of CO_2 in the domain with vertical and horizontal top boundary flux, respectively. With the vertical top boundary flux, there is advective inflow of water with a large CO_2 concentration into the domain. This causes larger concentrations in the fingers, which therefore travel faster. The fingers also form earlier, as can be expected from the linear stability results. Between the fingers, there are regions with low concentrations also adjacent to the top boundary, due to the upward flow of water through the boundary at those locations. With the horizontal top boundary flux on the other hand, the diffusion layer never disappears and the fingers form from very local feeding sites because the water is moving towards the feeding sites from both sides.

Next, we turn our attention to upscaled parameters such as the time development of the exponential growth rate and the dominant wavenumber. We define the growth rate as

$$\sigma(t) = \frac{1}{\Delta t} \ln \left(\frac{\bar{\bar{\omega}}(t)}{\bar{\bar{\omega}}(t - \Delta t)} \right), \tag{37}$$

where $\bar{\bar{\omega}}$ is the absolute value of the horizontal concentration gradient (vorticity), integrated horizontally and vertically across the domain. The development of the growth rate is shown in Fig. 8(a). At early times, the growth rates obtained with the 2D simulations resemble the growth rates obtained for the gravest mode in the linear stability analysis. There is a small delay between the linear dominant mode results and non-linear results with the vertical top boundary flux, however. From Fig. 4, we saw that different definitions of σ in the linear analysis gave different results. Based on the numerical solution to the linearized IVP, the onset time from the integral definition of σ is 50. This is more closely related
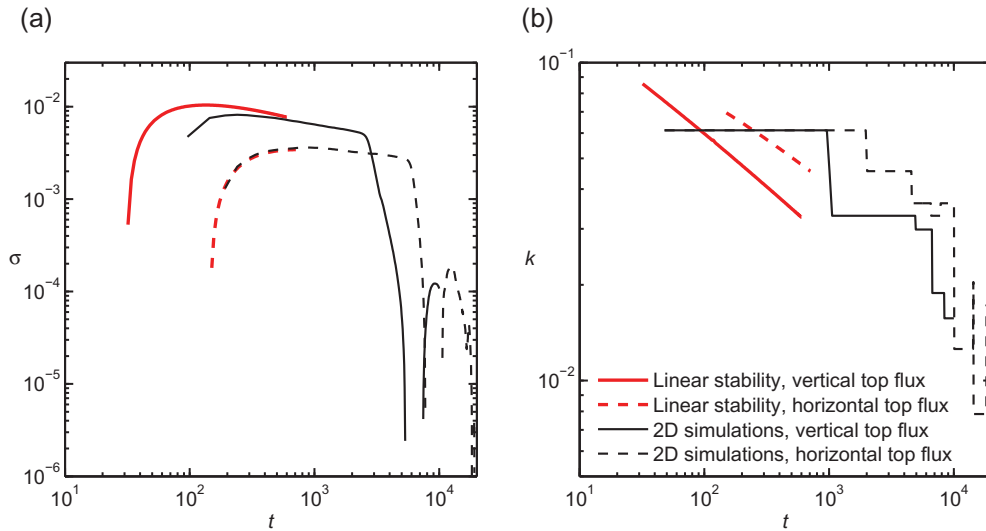
(a)

(b)

FIG. 8. (a) Growth rate versus time and (b) dominant wavenumber versus time for the vertical and horizontal top boundary flux. Linear stability results computed with the dominant mode method are shown in red for comparison.

to the non-linear results shown in Fig. 8(a). The delay may also be partly explained by the interaction between different modes in the 2D simulations. After onset, there is a period of exponential growth until the fingers move out of the diffusive boundary layer at $t \approx 2.6 \times 10^3$ and 6.0×10^3, respectively. It is shown clearly in Figs 6, 7 and 8(a) that non-linear effects start to dominate at these times.

The dominant wavenumber is defined from the vertically integrated concentration distribution $\bar{c}(x, t)$. First, we make this function periodic by mirroring it in $x = 0$. The resulting function is Fourier decomposed, and we define the Fourier component with largest amplitude to be the dominant wavenumber. In Fig. 8(b), the dominant wavenumbers of the 2D simulations with a random initial perturbation are displayed together with the most unstable wavenumbers from the linear stability analysis. At early times, the selection of modes obtained with the 2D simulations resemble the selection obtained with the linear stability analysis. Shortly after the fingers begin to penetrate below the diffusive boundary layer, the wavenumbers decrease more rapidly, corresponding to enhanced merging of fingers. We performed multiple realizations with different random initial conditions which give similar results as those displayed in Fig. 8.

In Fig. 9, the finger tip propagation and mass flux of CO_2 into the domain are given for several different random initial perturbations. Quantified values below are given as mean values. Figure 9(a) shows that the tip propagates as $\approx t^{1.6}$ in the convective regime with the vertical top boundary flux, with a faster speed initially and a slower speed towards the end. The mean value is the same with the horizontal top boundary flux, but with slower speed initially and a faster speed towards the end. In absolute values, the speed is twice as large with the vertical top boundary flux. This difference is due to enhanced concentrations in the fingers. In Fig. 9(b), the non-dimensional mass flux F over the top boundary is shown. It is related to the dimensional flux F_c as $F_c = F K_1 \Delta \rho g m / \mu$ where m is the CO_2 concentration at the solubility limit. The unit of F_c is kg $CO_2/(m^2 s)$. For comparison, the so-called Sherwood number is obtained by multiplying F by our non-dimensional domain thickness, which is what is usually referred to as the Rayleigh number, $Ra = K_1 \Delta \rho g H / (\mu \phi D)$. At approximate non-dimensional times 2.4×10^3
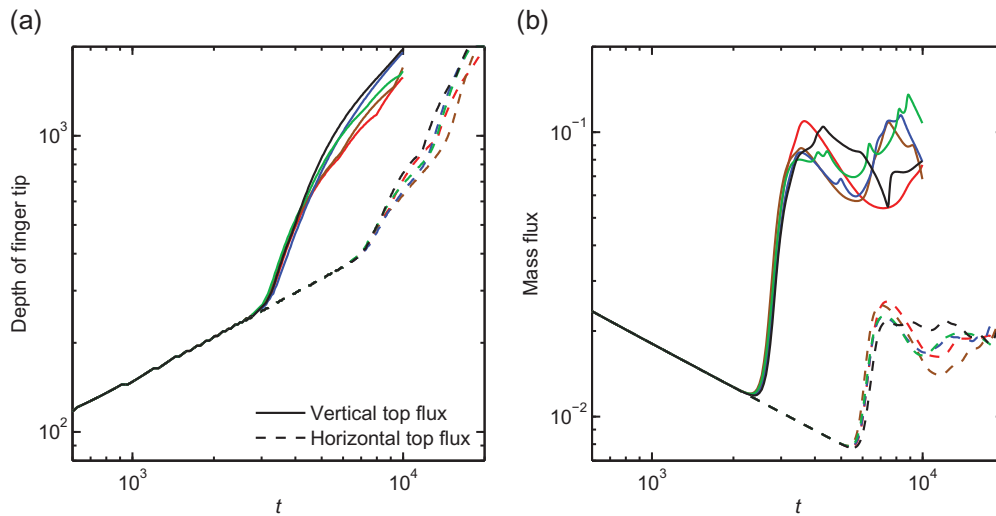
FIG. 9. (a) Depth of the finger tip defined as the lowest occurrence the concentration $c = 1 \times 10^{-3}$ and (b) mass flux across the top boundary. For each boundary condition, results for five different initial perturbations are presented.

and 5.4×10^3, respectively, there is a minimum in the mass flux. This is close to the times mentioned above regarding when the fingers leave the diffusive boundary layer. After these times, convective mixing is dominant. We measure the mean values of the mass flux from times 4.8×10^3 and 10.8×10^3, respectively, until the end of simulation. The mass flux with the horizontal top boundary flux is 0.020. This is at the lower end of the range of values presented by Neufeld *et al.* (2010) who also used the horizontal flux boundary condition at the top. The vertical top boundary flux leads to considerably larger mass flux of 0.075.

4. Discussion

We have shown that the cross-flow between the capillary transition zone and the diffusive boundary layer may reduce the onset time of instability by a factor of five. This result reflects that the onset occurs earlier in the development of the diffusive boundary layer. The critical wavelength of the instability is not strongly affected by the cross-flow, indicating that it is determined mostly by lateral diffusion. The situation may be illuminated by considering the vertical position of the critical mode relative to the interface between the capillary transition zone and the diffusive boundary layer. Figure 10 exemplifies this view. The left circle corresponds to the results here, with no resistance in the capillary transition zone (vertical flux at the interface). The central circle corresponds to the traditional case examined for example by Riaz *et al.* (2006) with infinite resistance in the capillary transition zone (horizontal flux at the interface). A more realistic case would feature flow directions containing both vertical and horizontal components, as illustrated by the right circle. If we assume that the flux field is perfectly circular as in the figure, and that the boundary layer becomes unstable when the concentration reaches a certain value c_s at the bottom of the modes, then from (16) the onset time can be approximated as,

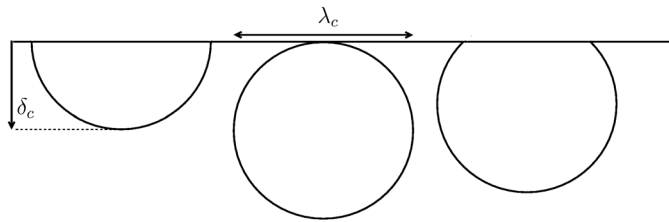$$t_c \approx \frac{\delta_c(c_s)^2}{4(\mathrm{erf}^{-1}(1 - c_s))^2}, \qquad (38)$$

FIG. 10. Positioning of modes with wavelength λ_c relative to the interface between the capillary transition zone and the diffusive boundary layer. The positioning of the three circles correspond to different amount of resistance to flow in the capillary transition zone, from left to right: no-resistance; infinite resistance; and some resistance.

where $\delta_c \in [\lambda_c/2, \lambda_c]$ is the thickness of the diffusive boundary layer. Equation (38) gives onset times 136 and 34 with vertical and horizontal top boundary flux, respectively, when $c_s = 1 \times 10^{-6}$ and a mean value of the critical wavelengths is used. These onset times closely resemble the results from the linear stability analysis; 146 and 31.

The analysis performed by Slim & Ramakrishnan (2010) displayed considerably more unstable flow than we have shown. When accounting for the flow between the capillary transition zone and the water region, they found an onset time that tends to zero and a wavelength that tends to infinity when the size of the domain is not limiting. Also for the no-flow top boundary which was studied before by Riaz *et al.* (2006), the system of Slim & Ramakrishnan (2010) is more unstable. They account the differences to the dominant mode method. However, since the results from the dominant mode method agree well with solutions of the full linear and the full nonlinear problems as shown here and by Riaz *et al.* (2006), this does not explain the differences. On the other hand, our usage of the similarity variable ξ in the linear analysis and the introduction of perturbations at the top nodes in the non-linear simulations leads to perturbations initiated close to the top boundary which is more realistic for many physical settings. The subsequent evolution of the perturbations introduced in this way is not restricted by the use of the variable ξ as shown by the agreement between linear stability results (with ξ) and the non-linear simulations (without ξ).

In our investigation, we have defined the onset time as the time when the first mode obtains a positive growth rate. This is a natural definition in the linear regime and as discussed above, it facilitates an intuition about the physical mechanisms. However, it should be noted that this definition may not be a good measure for other important features such as enhanced convective mixing. For instance, the onset time of the enhanced mixing depends on the size of the initial perturbations, but the time when the first mode obtains a positive growth rate does not.

5. Conclusions

Most previous stability investigations of diffusive boundary layers assume no-flux through the top boundary. In the case of CO_2 sequestration, this boundary represents the interface between the capillary transition zone and the diffusive boundary layer, and it is most realistic to assume some flux through the boundary. We have investigated this scenario. In the special case $\mathscr{K} \to \infty$, this model problem is considerably more unstable than the case where $\mathscr{K} \to 0$. Onset occurs earlier and the strength of convective mixing is larger. Since a realistic case would include both horizontal and vertical flow components, it appears that the relations for the onset time of perturbation growth and critical wavelength for the homogeneous stability problem with pure diffusion should lie within a range of values as given

TABLE 1 *Parameters motivated by Utsira and Krechba*

Parameter	Utsira	Krechba	Unit
K	2.5×10^{-12}	1×10^{-14}	m^2
ϕ	0.38	0.16	–
Injection	1×10^9	1×10^9	kg/year
Plume extent	$2\,t/3 \times 10^{6\dagger}$	$6 \times 10^{6\ddagger}$	m^2

[†]Our simplified formulae based on seismic observed total plume area under horizontal layers, presented by Boait *et al.* (2011). Here t is time in years after 1996 when injection began.
[‡]2011 simulated extent estimated from Cavanagh & Ringrose (2011).

in dimensional form by,

$$t_c \in \left[31 \frac{(\phi\mu)^2 D}{(K\Delta\rho g)^2}, 146 \frac{(\phi\mu)^2 D}{(K\Delta\rho g)^2} \right], \tag{39}$$

$$\lambda_c \in \left[\frac{2\pi\mu D\phi}{0.086 K\Delta\rho g}, \frac{2\pi\mu D\phi}{0.07 K\Delta\rho g} \right]. \tag{40}$$

For example, using data motivated by the Utsira formation (Sleipner field) in the North Sea (Bickle *et al.*, 2007; Neufeld *et al.*, 2010, Table 1), we may obtain onset of perturbation growth in the range 0.5–2 days, a critical wavelength of approximately 0.1 m and dissolution in 2011 corresponding to 14–52% of the injected amount CO_2 this year, if one assumes that the water column is not saturated with CO_2 anywhere under the plume(s). The time-integrated dissolution is estimated between 7 and 26% of all injected CO_2 (1996–2011) with this model. The small onset times and large dissolution rates are mainly related to the large permeability of the Utsira formation. The permeability is considerably lower at the Krechba field (In Salah) in Algeria. Using data motivated by this field (Mathieson *et al.*, 2009; Cavanagh & Ringrose, 2011; Table 1), we may obtain onset times in the range 20–80 years, a critical wavelength of approximately 15 m and dissolution in the range 0.03–0.1% of the annually injected CO_2. In both cases, we used $\Delta\rho = 10.5\,\mathrm{kg\ m^{-3}}$, $\mu = 5.9 \times 10^{-4}\,\mathrm{Pa\,s}$, $D = 2 \times 10^{-9}\,\mathrm{m^2\,s^{-1}}$ and $m = 50\,\mathrm{kg\,m^{-3}}$ dissolved CO_2 at the solubility limit, compare (Neufeld *et al.*, 2010). Again, note that the onset times given here mark the beginning of perturbation growth. The onset of enhanced convective mixing begins later and depends on the size of initial perturbations.

The large sensitivity in onset times and dissolution rates on the influence of the capillary transition zone call for a closer investigation. Knowledge of the range of time and length scales as provided in this article should be valuable also when investigating that problem.

Acknowledgements

Funding

References

BICKLE, M., CHADWICK, A., HUPPERT, H., HALLWORTH, M. & LYLE, S. (2007) Modelling carbon dioxide accumulation at Sleipner: implications for underground carbon storage. *Earth Planet. Sci. Lett.*, **255**, 164–176.

BOAIT, F., WHITE, N., CHADWICK, A., NOY, D. & BICKLE, M. (2011) Layer spreading and dimming within the CO_2 plume at the Sleipner Field in the North Sea. *Energy Proc.*, **4**, 3254–3261.

CAVANAGH, A. & RINGROSE, P. (2011) Simulation of CO_2 distribution at the In Salah storage site using high-resolution field-scale models. *Energy Proc.*, **4**, 3730–3737.

ELENIUS, M. T. (2011) Convective mixing in geological carbon storage. *Ph.D. Thesis*, submitted at the University of Bergen, Norway.

ENNIS-KING, J. P. & PATERSON, L. (2003) Role of convective mixing in the long-term storage of carbon dioxide in deep saline formations. *SPE*, 84344.

ENNIS-KING, J. P., PRESTON, I. & PATERSON, L. (2005) Onset of convection in anisotropic porous media subject to a rapid change in boundary conditions. *Phys. Fluids*, **17**, 084107.

FARJAZADEH, R., RANGANATHAN, P., ZITHA, P. L. J. & BRUINING, J. (2011) The effect of heterogeneity on the character of density-driven natural convection of CO_2 overlying a brine layer. *Adv. Water Resour.*, **34**, 327–339.

FEIN, E. (1998) d^3f-Ein Programmpaket zur Modellierung von Dichteströmungen. *GRS, Braunschweig, GRS-139*.

FOLLAND, G. B. (1992) *Fourier Analysis and its Applications*. Brooks/Cole Publishing Company.

FOSTER, T. D. (1968) Effect of boundary conditions on the onset of convection. *Phys. Fluids*, **11**, 1257–1262.

HESSE, M. A. (2008) Mathematical modeling and multiscale simulation for CO_2 storage in saline aquifers. *Ph.D. Thesis*, Stanford University, USA.

HIDALGO, J. J. & CARRERA, J. (2009) Effect of dispersion on the onset of convection during CO_2 sequestration. *J. Fluid Mech.*, **640**, 441–452.

IPCC (INTERGOVERNMENTAL PANEL ON CLIMATE CHANGE). (2005) *Special report on carbon dioxide capture and storage*.

JOHANNSEN, K. (2004) Numerische Aspekte dichtegetriebener Strömung in porösen Medien. *Professorial dissertation (habilitation)*. Germany: Heidelberg.

KNEAFSEY, T. J. & PRUESS, K. (2010) Laboratory flow experiments for visualizing carbon dioxide-induced, density-driven brine convection. *Transp. Porous Med.*, **82**, 123–139.

LINDEBERG, E. & WESSEL-BERG, D. (1997) Vertical convection in an aquifer column under a gas cap of CO_2. *Energy Convers. Manage.*, **38**, 229–234.

MATHIESON, A., WRIGHT, I., ROBERTS, D. & RINGROSE, P. (2009) Satellite imaging to monitor CO_2 movement at Krechba, Algeria. *Energy Proc.*, **1**, 2201–2209.

NEUFELD, J. A., HESSE, M. A., RIAZ, A., HALLWORTH, M. A., TCHELEPI, H. A. & HUPPERT, H. E. (2010) Convective dissolution of carbon dioxide in saline aquifers. *Geophys. Res. Lett.*, **37**, L22404.

NIELD, D. A. & BEJAN, A. (2006) *Convection in Porous Media*. New York: Springer.

PAU, G. S. H., BELL, J. B., PRUESS, K., ALMGREN, A. S., LIJEWSKI, M. J. & ZHANG, K. (2010) High-resolution simulation and characterization of density-driven flow in CO_2 storage in saline aquifers. *Adv. Water Resour.*, **33**, 443–455.

PINDER, G. F. & CELIA, M. A. (2006) *Subsurface Hydrology*. New York: John Wiley and Sons.

PRUESS, K. & ZHANG, K. (2008) Numerical modeling studies of the dissolution–diffusion–convection process during CO_2 storage in saline aquifers. *Technical Report LBNL-1243E*. USA: Lawrence Berkley National Laboratory.

RIAZ, A., HESSE, M., TCHELEPI, H. A. & ORR, F. M. (2006) Onset of convection in a gravitationally unstable diffusive boundary layer in porous media. *J. Fluid Mech.*, **548**, 87–111.

ROBINSON, J. L. (1976) Theoretical analysis of convective instability of a growing horizontal thermal boundary layer. *Phys. Fluids*, **19**, 778–791.

SLIM, A. C. & RAMAKRISHNAN, T. S. (2010) Onset and cessation of time-dependent, dissolution-driven convection in porous media. *Phys. Fluids*, **22**, 124103.

XU, X., CHEN, S. & ZHANG, D. (2006) Convective stability analysis of the long-term storage of carbon dioxide in deep saline aquifers. *Adv. Water Resour.*, **29**, 397–407.

YANG, C. & GU, Y. (2006) Accelerated mass transfer of CO_2 in reservoir brine due to density-driven natural convection at high pressures and elevated temperatures. *Ind. Eng. Chem. Res.*, **45**, 2430–2436.